



Chinese Society of Aeronautics and Astronautics  
& Beihang University

Chinese Journal of Aeronautics

cja@buaa.edu.cn  
www.sciencedirect.com



# Study of geometric parameters for the design of short intakes with fan modelling

Andrea MAGRINI\*, Ernesto BENINI

*Dipartimento di Ingegneria Industriale, Università degli Studi di Padova, Padova 35131, Italy*

Received 25 September 2021; revised 24 October 2021; accepted 29 November 2021

Available online 1 February 2022

## KEYWORDS

Body force method;  
Coupled methods;  
Fan/intake interaction;  
Nacelle aerodynamics;  
Short intake;  
UHBPR

**Abstract** The flow over a short intake is characterised by a strong interaction with the fan, that can only be captured when the rotor blades are modelled in the numerical simulations. In this paper, we use a coupled methodology to derive indications about relevant geometric variables affecting the high-incidence operation of an ultra-high bypass ratio turbofan intake with a length-to-diameter ratio of 0.35. By reproducing the effect of the fan through a body force model, we carry out a parametric study of the influence of the contraction ratio and the scarf angle at take-off conditions for a grid of 28 different three-dimensional shapes. The analysis of the selected performance metrics distributions at three angles of attack of 16°, 24°, and 28° reveals that a contraction ratio higher than 1.20 is needed to avoid separation at high incidence. While for an attached inlet the best performance is found with a moderate scarf angle, in presence of a developed separation the distortion level reduces as the scarf decreases up to negative values. We discuss the correspondence between the distortion indexes and the flow field, highlighting the origin of the detachment for the different geometries, according to the operating condition, and analysing the fan operation in the most distorted case. Finally, we assess the influence of modelling the rotor in the simulations, showing that its suppression effect on the separation at a given incidence depends on the intake geometric features.

© 2022 Chinese Society of Aeronautics and Astronautics. Production and hosting by Elsevier Ltd. This is an open access article under the CC BY-NC-ND license (<http://creativecommons.org/licenses/by-nc-nd/4.0/>).

## 1. Introduction

The mid-term evolution of civil podded engines is progressing towards the adoption of increased bypass ratio units, tackling a mitigation of the environmental impact of the aviation sector through improved propulsive efficiency, reduced fuel burn and noise footprint.<sup>1–3</sup> The enlargement of the engine fan size and the overall weight is compensated by more aggressive nacelle

designs, featuring a compact cowl to limit the weight and drag.<sup>4</sup> On the intake side, a contemporary reduction of the duct length is sought. The decreased wall friction losses, however, are counterbalanced by the enhanced interference with the fan.<sup>5</sup>

Fan/intake interaction at high incidence has been widely studied in experimental tests and numerical studies. Wind tunnel measurements highlighted the distortion attenuation effect on the inlet flow by the fan and the extension of the attached operation due to the coupling.<sup>6–8</sup> Coschignano et al.<sup>9,10</sup> investigated the effect of the lip shape on shock/boundary layer interaction, finding that the post-shock diffusion can

\* Corresponding author.

E-mail addresses: [andrea.magrini@unipd.it](mailto:andrea.magrini@unipd.it) (A. MAGRINI), [ernesto.benini@unipd.it](mailto:ernesto.benini@unipd.it) (E. BENINI).

<https://doi.org/10.1016/j.cja.2022.01.018>

1000-9361 © 2022 Chinese Society of Aeronautics and Astronautics. Production and hosting by Elsevier Ltd.

This is an open access article under the CC BY-NC-ND license (<http://creativecommons.org/licenses/by-nc-nd/4.0/>).

deteriorate the boundary layer and prevent reattachment. Kennedy et al.<sup>11</sup> compared steady RANS simulations of a long intake at incidence with wind tunnel data, both in the intake-alone and the fan-modelled case, recommending the inclusion of the rotor when considering unfavourable operating conditions to capture the upstream flow redistribution and the separation onset delay.

These studies were related to conventional intake designs, characterised by a ratio between the duct length and the fan face diameter  $L/D$  above 0.5. For more compact configurations, the mutual effect of the fan on the inlet, and vice versa, is exacerbated. Fundamental physical mechanisms characterising this interaction are provided by time-accurate simulations, capturing the unsteady coupling, the different timescales involved, and the time-averaged operating point.

Cao et al.<sup>12</sup> carried out URANS simulations of three-dimensional intakes with progressively lower  $L/D$ , from 0.44 to 0.14, including the fan rotor blades. Compared to a flow-through case, the relative separation level attenuation was found to be 60%-70%, regardless of the duct length. This was attributed to the mass flux redistribution imposed by the rotor. The fan suction decays rapidly upstream, causing the separation angle extension to range from  $5^\circ$  for  $L/D = 0.17$  to  $0^\circ$  for  $L/D$  of 0.44. Vadlamani et al.<sup>13</sup> described the influence of the intake on the fan operation in terms of streamline curvature and upwash. The first feature is related to the turning of the streamtube from the freestream to the inlet axis direction. It brings a vertical pressure gradient, with lower pressure, high turning, and mass flux at the bottom, and higher pressure, lower curvature, and mass flux at the top. The second is related to the incomplete flow straightening, especially near the bottom dead centre, leaving an upward velocity component at the fan face. Both effects combine together to change the axial or swirl velocity, altering the velocity triangles and the fan working point over the whole interface plane.

Mohankumar et al.<sup>14</sup> identified three mechanisms affecting thrust and work input in a short intake with  $L/D = 0.35$ : rotor choking loss, rotor-separation interaction, and radial flows. Gunn et al.<sup>15</sup> compared a conventional and short intake at cruise and high incidence using URANS. The authors found that, compared to a conventional design, the short intake always increases the non uniformity at the fan. At high incidence, the flow turning must occur in a smaller space for the former, leading to increased streamline curvature and acceleration near the lip, with a stronger normal shock. The separation built up more smoothly in the short intake and appeared earlier. The rotor blades were able to recover after going through the distortion, which allows to avoid rotating stall instability.<sup>16</sup> The amplitude of the recovery region downstream of the fan was found to be smaller for the short case.

The published research on short intakes simulations highlights the strong coupling effect with the fan rotor, whose absence in the computational domain leads to unphysical results. From a numerical standpoint, this requires time-accurate analyses of full-annulus configurations, where the rotating fan and stationary downstream components must be included, as they can alter the distortion response.<sup>17,18</sup> In order to alleviate the computational burden of this expensive simulations, lower order fan models have been devised. Ma et al.<sup>19</sup> used an implicit method derived from the immersed boundary, called Immersed Boundary Method with Smeared Geometry (IBMSG), to mimic the fan operating behind a wedged

distortion generator. With the fan model active, the difference between RANS and Large Eddy Simulations (LES) was substantially mitigated and reduced progressively as the blade distance from the distortion generator decreased, indicating that the mass flow redistribution imposed by the rotor has a dominant effect on the solution. Carnevale et al.<sup>20</sup> exploited a transonic fan similarity model that can be used for steady or unsteady solutions and was found to provide a good approximation of the URANS solution.

Among the different classes of methods, Body Force Models (BFM) have been used quite successfully as a flow-coupled fan representation. This three-dimensional throughflow approach is based on mass, momentum and energy source terms distributions added to the Navier-Stokes equations, amounting to the circumferential and time averaged effect of a blade row on the flow.<sup>21</sup> Burlot et al.<sup>22</sup> compared URANS with steady RANS, a body force and an Actuator Disk (AD) model for an Ultra-High Bypass Ratio (UHBPR) engine with a short intake featuring an  $L/D \approx 0.3$ , at cruise and take-off conditions. They concluded that only the BFM was able to capture the flow redistribution and the distortion transfer across the fan and Outlet Guide Vanes (OGV) predicted by URANS and that full-wheel simulations are necessary to have realistic estimates of the machine performance. Godard et al.<sup>23</sup> conducted a similar study with steady RANS, BFM, and AD to reproduce an experimental test of the MASCOT2 engine operating at crosswind. The subsonic separation limit for the long intake ( $L/D \approx 0.6$ ) was well captured by the BFM, which instead suffered from a greater bias with measurements at high crosswind velocity or rotational speed, proving however the good potential of the method. Benichou et al.<sup>24</sup> also highlighted good duplication of URANS for a low-speed cooling fan in presence of a  $180^\circ$  distortion, reporting a time saving factor of 40 using the BFM.

The above research was mostly related to the study of key physical features of the fan/intake problem focusing on the engine side. They identified the mechanisms of fan response to the distortion caused by high-incidence inlet operation and its predominant influence on the intake mass flux. The deeper understanding of the phenomena driving the fan work input and the stage losses made possible by time-resolved simulations builds the basis for the design of advanced distortion-tolerant blades. On the intake side, however, less information is present. Considering UHBPR engines, the optimisation of nacelle cowl and exhaust duct is reported in several works,<sup>25</sup> but less evidence of dedicated intake design studies is present, especially for short configurations.

Yeung et al.<sup>26</sup> isolated a portion of a 3D ingested streamtube to study the intake flow with a quasi-3D approach to reduce the computational weight. The strategy reproduces the main trends in the case of attached flow, but the tube shape depends upon the mass flow rate. John et al.<sup>27</sup> used shock control bumps to increase the separation incidence of the inlet up to three degrees. Wang et al.<sup>28</sup> presented a parametric tool including three-dimensional design parameters to be used in shape optimisation. Abbott<sup>29</sup> carried out a systematic analysis on negatively scarfed intakes, studying the effect of the circumferential extent over which the scarf is applied, building a database of configurations matching a specified lip stall angle.

In the context of an increased engine integration and the growing interest in Boundary Layer Ingestion (BLI) propulsion, the development of fully coupled design methodologies

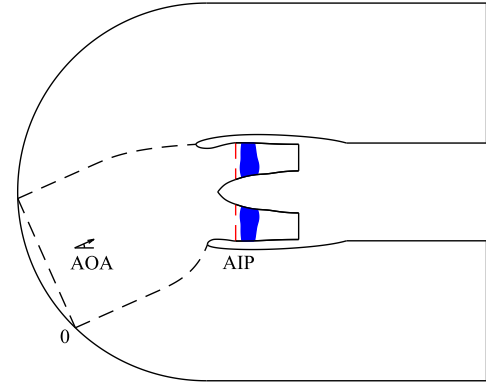
represents an essential step for the successful achievement of system performance improvements.<sup>30</sup> The literature research on fan/intake interaction has unequivocally proven the need to consider the mutual component influence at design level. This is especially true in case of shorter ducts or BLI propulsion.<sup>15,31</sup> Few attempts on this objective are publicly reported. Peters et al.<sup>5</sup> investigated several aspects of short intakes using a BFM, providing quantitative estimates of the potential improvements. Through manual lip design for multiple operating points, the author postulated that a balanced trade-off between fan efficiency degradation and nacelle drag reduction is present at  $L/D \approx 0.35$ . Corroyer and Schnell<sup>32</sup> carried out a multi-objective coupled optimisation in terms of fan efficiency at cruise and pressure ratio at two take-off points for an  $L/D \approx 0.35$  intake using URANS. The selected optimised sample featured a larger highlight area and a slimmer lip. In a past study,<sup>33</sup> we examined the sensitivity of high-incidence aerodynamics to the design parameters of conventional axisymmetric intakes using a body force model for the rotor. Yildirim et al.<sup>34</sup> used the BFM for the coupled optimisation of a BLI podded propulsor.

Progressing towards a more integrated approach, in this paper we present a parametric study of the influence of some key geometric variables for three-dimensional short intakes using a coupled fan model based on the body force method. The scope of the research is (A) to present a method to study future UHBPR engines short inlets fully accounting for the rotor/inlet interaction; (B) to evaluate the effect of different three-dimensional parameters on the inlet operation at take-off; (C) to provide design guidelines on suitable sets of variables ensuring good intake/fan compatibility at high incidence. The study will contribute to the development of coupled methodologies for the aerodynamic design and analysis of integrated systems in the framework of traditional podded engines and BLI propulsors.

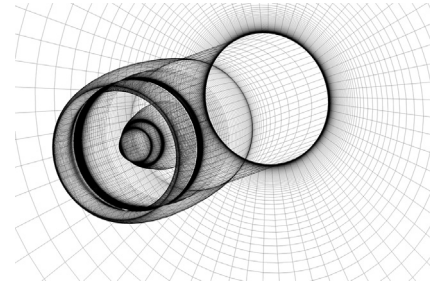
## 2. Methods

The numerical methods used for the simulation of nacelle intakes and engine blades are based on steady RANS solutions using the Spalart–Allmaras turbulence model.<sup>35</sup> In the absence of open experimental data on powered intake flows, the inlet and the engine domains mesh were created by transferring point distributions obtained from separate validations of intake-alone and engine machine performance. The complete computational domain is schematised in Fig. 1. It comprised a three-dimensional nacelle and the fan rotor. The model was supported by a cylindrical sting. Freestream boundary conditions were imposed on the far-field, while the static back-pressure was set at the fan nozzle outlet. Station 0 represents the far-upstream capture section. In the following, flow variables with a zero subscript are taken at this section.

The fully structured multi-block mesh depicted in Fig. 2 was generated using Pointwise commercial software.<sup>36</sup> The intake gridding guidelines were derived from validation of experimental datasets for NACA 1–85 axisymmetric inlets.<sup>37</sup> Examples of the computed wall pressure coefficient  $C_p$  distribution along the chord normalised abscissa  $x/c$  are reported in Fig. 3 for two Mach numbers  $Ma$  and Mass Flow Capture Ratio (MFCR) (Eq. (4)). The mesh sensitivity was assessed through systematic refinement with a ratio of 1.414 on three



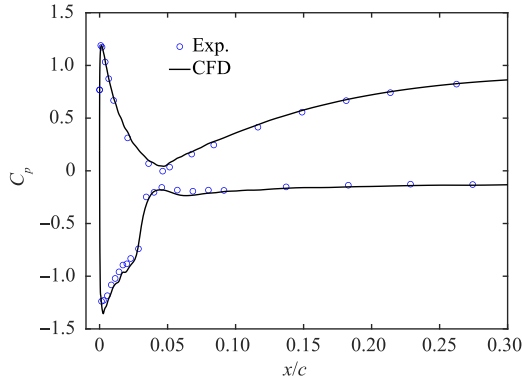
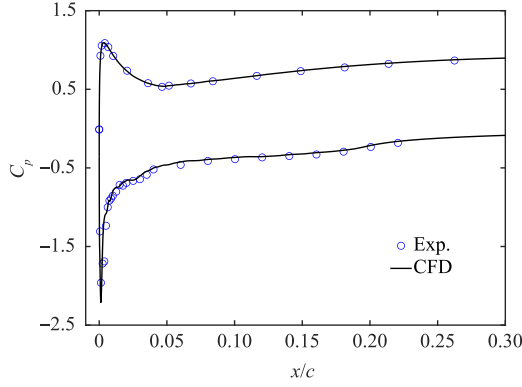
**Fig. 1** Schematic of computational domain used in study (the volume swept by the rotor where the body forces are active is shown in blue; the plane on which the metrics are evaluated (Aerodynamic Interface Plane, AIP) stands in front of the fan and is indicated with the dashed red line).



**Fig. 2** Multi-block structured grid.

grid levels. Negligible differences between them were found. The Grid Convergence Index (GCI)<sup>38</sup> of total pressure at the measurement plane was largely lower than 0.1% from the medium to the fine grid in all operating points tested and the medium point distribution was retained as a baseline for the three-dimensional cases.

The influence of the grid size and the mesh parameters for the nacelle geometries tested in the study was ascertained in a detailed analysis. The number of points in blade region was set by the engine modelling requirements deriving from BFM validation reported in the next subsection. For this reason, it was not changed during the mesh sensitivity study. All other distributions were varied systematically by applying a uniform refinement factor of 1.414, which resulted in three mesh levels: coarse (C), medium (M), and fine (F), having a total number of elements of 3.73, 6.35, and 12.31 million, respectively. Fig. 4(a) shows total pressure distributions along the circumferential direction  $\theta$  at 20% and 95% of span for the three levels at an angle of attack of  $24^\circ$ . The profiles collapse progressively as the mesh size is increased and the maximum absolute local difference is 0.1% of freestream total pressure from C to F. The ratio between the area-averaged total pressure  $p_0$  close to the fan face and a reference value  $p_{0ref}$  at different angles of attack are depicted in Fig. 4(b), where it can be appreciated the little variation between the grids also at higher incidence. Seeking an optimum balance between computational time and grid convergence, the medium mesh level was used everywhere in the study.

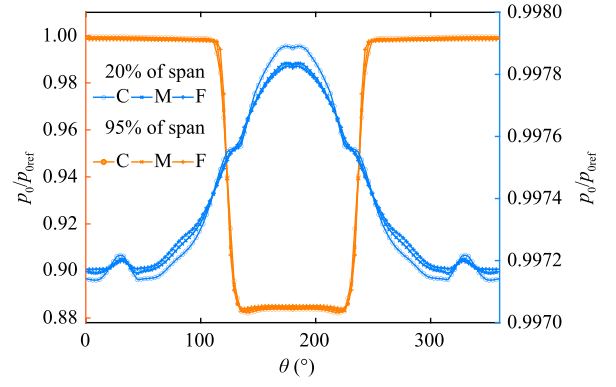
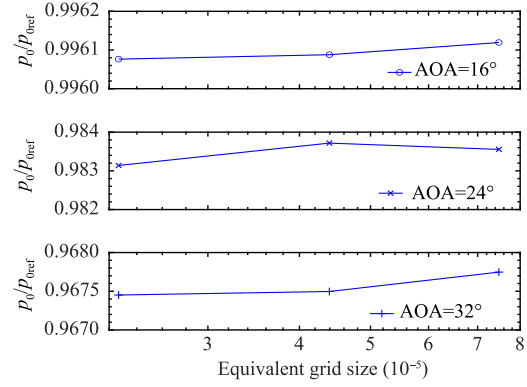
(a) NACA 1-85-100,  $Ma=0.84$ ,  $MFCR=0.74$ (b) NACA 1-85-43.9,  $Ma=0.60$ ,  $MFCR=0.56$ **Fig. 3** Examples from NACA series 1 intake validations.

### 2.1. Body force modelling

As mentioned in the introduction, body force models are based on the application of source terms in the right-hand side of the Navier–Stokes equations to reproduce the effect of the blades on the flow. The formulation here employed was based on the  $L/D$  model of Thollet,<sup>39</sup> with some modifications. The final expression of the force components in the  $L/D$  model is reported in Eq. (1) for clarity. It relies on local flow variables (the relative velocity magnitude  $W$  and the relative velocity angle  $\beta$ ), blade geometric parameters through the row solidity  $\chi$  and the staggered pitch  $\tilde{h}$ , and local calibration coefficients  $\beta_n^0, \beta_p^0, K_p^0$  that are instructed from standard 3D CFD simulations of the machine blades.

$$\begin{cases} f_n = \frac{2\pi\chi}{\tilde{h}} (\beta - \beta_n^0) \\ f_p = \frac{K_p}{\tilde{h}} W^2 \\ K_p = K_p^0 + 2\pi\chi (\beta - \beta_p^0)^2 \end{cases} \quad (1)$$

The numerical implementation followed the indications coming from a separate research,<sup>40</sup> where we conducted a thorough investigation including the definition of optimal calibration procedures, the normal force application to account for blade lean and sweep, the validation at different flight conditions, and the application to fan/intake problems. The methodology was validated for the NASA R4 stage, exploiting the large number of experimental data available for the transonic high-bypass rotor with OGVs. The results of this activity are

(a) Circumferential distribution of total pressure at  $AOA=24^\circ$ 

(b) Total pressure sensitivity to mesh size at different angles of attack

**Fig. 4** Summary of mesh sensitivity study for intake + BFM.

here summarised, starting from the fan characteristic maps of Fig. 5(a), given against the corrected mass flow rate  $\dot{m}_c$ . Experimental data taken in the NASA GRC  $9 \times 15$  ft (1ft = 0.3048 m) wind tunnel<sup>41</sup> are compared with single-passage steady CFD and the corresponding body force model in terms of Total Pressure Ratio (TPR) and isentropic efficiency  $\eta_{iso}$  at the design corrected rotational speed. Both numerical curves are well overlapped with the measured data points and closely capture the experimental trends. The slope of the pressure rise line at lower mass flow in the BFM is even closer to the experimental one. An almost constant offset in the efficiency value is present, which is a known limitation of the model and derives from choking mass flow calibration.

Spanwise profiles of total pressure ratio of the rotor for the complete stage simulation on the take off operating line at full thrust are depicted in Fig. 5(b). Experimental points were taken in two different campaigns in the  $9 \times 15$  ft and W8 NASA wind tunnels.<sup>42</sup> The CFD profile falls between the experimental curves. The BFM replicates well the spanwise distribution, with a slightly higher compression in the upper span of the blade. The adherence between the data sets highlights the good resolution of the adopted body force formulation and validates its implementation.

### 2.2. Performance metrics

The metrics analysed to rank the intake samples were based on the total pressure loss on the intake duct and distortion

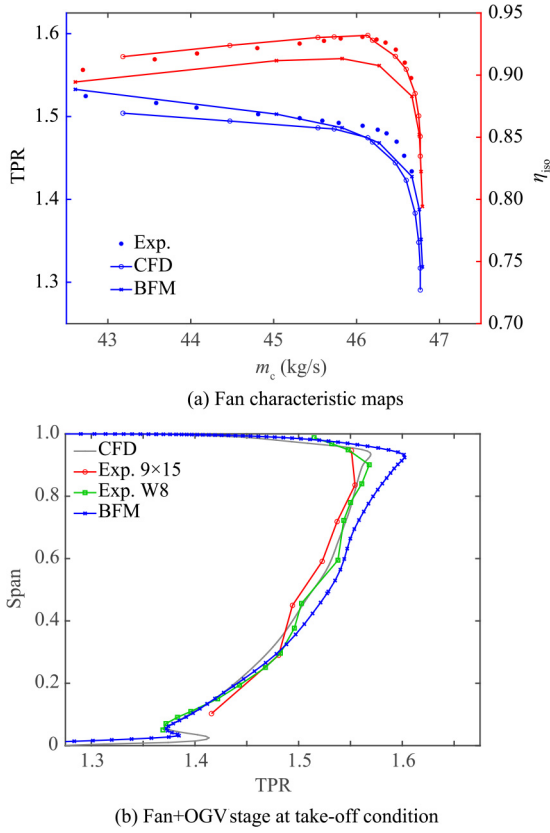


Fig. 5 Validation of NASA R4 transonic fan.

descriptors. All values were taken at the Aerodynamic Interface Plane (AIP), located close upstream of the rotor leading edge.<sup>43</sup> The Inlet Pressure Recovery (IPR) measured the average total pressure on the AIP  $p_{0,AIP}$ , relative to the freestream total pressure  $p_{0,0}$ :

$$IPR = p_{0,AIP}/p_{0,0} \quad (2)$$

The distortion can be evaluated in different ways. The SAE ARP 1420 document<sup>44</sup> defines a way of quantifying the swirl and total pressure distortion using values computed on a rake grid placed on the AIP. An industry-standard total pressure index is  $DC(\theta)$ , defined as the ratio between the area-averaged total pressure in the most distorted sector of amplitude  $\theta$  and the AIP dynamic pressure.<sup>45</sup> In the study, both criteria were used. While  $DC(60)$  has been widely reported as distortion index and has the advantage of giving a single value, rather than one on each radial level like the SAE's intensities, it is not sensitive to axisymmetric patterns and is less suitable for mixed radial and circumferential profiles.

With the purpose of overcoming the limitations of such descriptors based on coarsely grid-sampled values, Gunn et al.<sup>15</sup> proposed to evaluate the fan distortion by comparing the spoiled inflow with the corresponding clean case using an integral delta descriptor:

$$\overline{D}_q(\phi) = \frac{1}{q_{dist}} \int |\phi_{clean} - \phi_{dist}| dq \quad (3)$$

where  $\phi$  is the quantity whose distortion is measured from the clean ( $\phi_{clean}$ ) to the distorted ( $\phi_{dist}$ ) distribution, and  $q$  is the area, for an area-averaged descriptor, or the mass flow, for a

mass-flow-averaged descriptor. The  $\overline{D}_q$  operator can be applied either to total pressure or swirl and quantifies how different is the inflow condition of the distorted fan, compared to the design clean case. In the analysis, we employed  $\overline{D}_m(p_0)$  and  $\overline{D}_m(\alpha)$ , where  $\alpha$  represents the absolute swirl angle. The reference condition was the corresponding AIP distribution for an axisymmetric simulation of the ducted fan with clean inflow at the design operating point.

### 2.3. Test case and operating conditions

The research pertains to an UHBPR engine test case. The nacelle geometry was drawn from indications reported on the published literature to be representative of a compact and slim design for a tight underwing installation. It featured a ratio between the cowl length and the highlight radius  $L_{nac}/R_{hl} \approx 3.0$  and the maximum cowl thickness  $R_{max}$  was around  $1.14R_{hl}$ . The intake had a fixed  $L/D$  value of 0.35. As mentioned above, this ratio was postulated to offer a good balance between increased distortion and reduced drag, and it was chosen by many other authors. The bypass stage was designed for a pressure ratio  $< 1.45$ , with a cruise specific thrust  $< 80$  N/(kg·s) and a nominal bypass ratio  $> 15$ .

The study focused on the take-off condition, conducting an angle of attack sweep from  $16^\circ$  to  $28^\circ$ , ranging from take-off rotation to wing maximum lift. The freestream Mach number was 0.25. In all simulations, only the rotor blades were modelled. The attributes of inviscid interaction with the inlet were considered predominant on a more complete engine response evaluation for the purpose of intake geometries analysis, which can be captured with the rotor alone.

When using a responsive engine model fully linked to the flow field, the specification of the boundary conditions is not as direct as in the typical decoupled approach. Two aspects must be considered. The first is related to the engine side. The average operating point derives from the losses on the wall ducts, the energy and momentum exerted on the fluid by the rotor, and the conditions downstream of the stage. The final point on the characteristic map comes from the coupling between the intake flow and the deriving total pressure rise realised by the fan, as well as the efficiency of this work exchange. With a choked nozzle, the only controllable parameters are the throat area and the corrected rotational speed. For a given rotational speed, the operating point results from the intersection of the operative line with the corresponding speedline. In presence of an inflow distortion, however, in general the speedline shape changes and it is not possible to recover a priori the design operating condition.

The second aspect is related to the intake. The nacelle and inlet flow is characterised by the Mass Flow Capture Ratio (MFCR):

$$MFCR = \frac{A_0}{A_{hl}} = \frac{\dot{m}}{\rho_0 V_0 A_{hl}} \quad (4)$$

expressed as the ratio between the far-upstream streamtube capture area  $A_0$  and the highlight area  $A_{hl}$ , with  $\dot{m}$  the inlet mass flow,  $V_0$  the undisturbed velocity, and  $\rho_0$  the undisturbed density. When considering different inlet shapes, the comparison must be done at equal MFCR, as it influences the streamtube curvature around the lip and the stagnation point position. If the highlight area and the freestream conditions

are left unchanged, this is equivalent to keep the inlet mass flow fixed. Since the research was focused on the intake side, we chose to conduct the analysis at a constant mass flow giving a MFCR around 1.55, which is typical of a take-off condition.

Differently from the typical CFD approach where the engine is only modelled through boundary conditions set at the fan face outflow plane in terms of flow rate, in presence of a fully coupled flow field the fan/intake compatibility must be ensured. The intake geometry must be such that it allows the fan to reach the desired operating condition, providing sufficient flow capacity and minimising the distortion, to avoid total pressure and efficiency losses, or stall margin degradation. In the study, we equalised the mass flow across the different intake geometries by using an unchoked nozzle downstream of the fan and a floating static average backpressure that was changed during the CFD iterations until the target mass flow was reached. The pressure was updated after a fixed block of iterations and the procedure was stopped when the mass flow variation remained within 0.1% of the target value for at least two consecutive blocks. With a uniform pressure level at the outflow nozzle plane, or with a choked nozzle, the mass flow rate would have been a result of the flow coupling, giving a different MFCR for each intake geometry. The compatibility with the engine design operating condition was checked a posteriori, controlling an ideal thrust coefficient. The ideal engine thrust was computed as the gauge stream function variation from the far-upstream streamtube section to an ideal plane far downstream of the fan. The flow status on this plane was derived by assuming loss-free absolute swirl removal after the rotor and isentropic expansion to free-stream ambient static pressure  $p$ . The axial thrust coefficient  $CF_x$  was finally expressed as:

$$CF_x = \frac{\dot{m}(V_x^{\text{iso}} - V_0 \cos(\text{AOA}))}{A_0 p_{0,0}} \quad (5)$$

where  $V_x^{\text{iso}}$  is the ideal axial velocity after the isentropic nozzle expansion.

#### 2.4. Intake model and design parameters

The intake models tested were controlled by a fully parametric geometric tool. The procedure for model generation started from two-dimensional axisymmetric definition. The intake geometric parameters in this case are shown in Fig. 6. The highlight and fan face areas were fixed. The contraction ratio

$CR = A_{hl}/A_{\text{throat}}$  and the lip aspect ratio  $AR = a/b$  were directly controlled. The diffuser length and its wall angle  $\gamma$  resulted from the specified set of previous parameters.  $\gamma$  was expressed either in local terms, representing the diffuser curve slope on a  $z - r\theta$  plane, or in average terms, as the slope of the segment connecting the throat point with the casing at the fan face. The three-dimensional inlet shape derived from the application of azimuthal laws setting the distributions of CR and AR, centreline droop  $\delta$ , and highlight scarf  $\sigma$  angles, Fig. 6 (b). The circumferential evolution of the first two parameters was controlled via smooth cubic functions, ensuring symmetry with respect to a vertical meridional plane and continuity on the bottom and top dead centres. The functional form was kept unchanged as a design groundrule, while controlling the values at the circumferential coordinates  $\theta = 0$  (top dead centre) and  $\theta = \pi$  (bottom dead centre), to limit the number of free variables. After the revolution around the engine axis, the contoured intake was morphed by the droop angle  $\delta$ , measured as the offset between the engine and the inlet centreline. Finally, the geometry was scarfed by rotating the highlight plane around its top dead centre. For drooped shapes, CR and AR were computed in the direction normal to the rotated inlet axis. The introduction of scarf alters their distributions, compared to the axisymmetric definition, as the intake length is changed across  $\theta$ . The droop, conversely, is a pure rotation for the intake duct far from the fan face, but it modifies the external cowl forebody shape.

The number of design variables to be adopted to describe the three-dimensional intake shape is potentially high. Having fixed the  $L/D$  ratio and the highlight radius, the geometry is specified through the values of CR, AR, the azimuthal laws determining their variation, and the two angles  $\delta$  and  $\sigma$ . Controlling only the two circumferential positions at  $\theta = 0^\circ$  and  $\theta = 180^\circ$ , a total of six variables is needed, which is still practical in parametric analyses. When applying the set of variables chosen, the initial shape was modified by appropriate rescaling of the parametric curves defining the baseline geometry. No strict local curve control was therefore applied, as this would require acting explicitly on the mathematical curve functional, largely increasing the number of variables needed. The parametric study was rather aimed at identifying a suitable set of geometric parameters for the high-incidence operation of a three-dimensional short intake model.

### 3. Results

The first investigation was a design space exploration, carried out to capture the main trends between the design variables and the performance metrics and select the search bounds for the following analyses. The Design of Experiment (DOE) involved the independent variation of the crown and keel profiles for 100 individuals. A fixed incidence of  $16^\circ$  was studied. The regions where a lip separation appears, in fact, are also to be avoided when operating at a larger angle of attack. The intake  $L/D$  ratio was not changed, as well as the droop angle  $\delta$ . This latter, in fact, is mainly set to align the inlet axis with the freestream velocity at cruise, compensating for the engine pitch installation angle,<sup>46</sup> and it was regarded as a constrained variable.

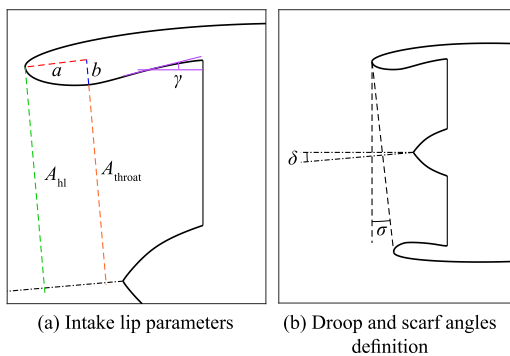


Fig. 6 Geometric parameters for intake definition.

### 3.1. Preliminary DOE exploration

The results of the DOE are summarised in Fig. 7 for the IPR and DC(60) index distributions versus geometric parameters. The subscript denotes the circumferential position  $\theta$  ( $0$  = top dead centre,  $\pi$  = bottom dead centre). The scarf angle acts to reduce the duct length from the highlight to the fan face towards the bottom dead centre when positive. Values in excess of  $3.5^\circ$  are shown in the figure to be associated to a trend of reduced IPR and enhanced DC(60). The lip AR, in contrast, was not found to correlate with the metrics at none of the circumferential positions (here only  $\theta = \pi$  is shown). On the bottom dead centre, higher total pressure losses and circumferential distortion appeared for  $AR < 1.5$ , with an almost independent effect for higher values. A similar trend can be noticed for the contraction ratio.  $CR_0$  presented a region of slightly reduced IPR when above 1.3, with a weaker effect on DC(60). At  $\theta = \pi$ , low losses and distortion level were measured almost across the whole range tested. On the bottom row of Fig. 7, the average wall diffuser angle on the crown and keel profiles is reported. This parameter derives from the direct imposition of CR, AR, and  $\sigma$ . The bottom section seemed to be more tolerant to highly diffusing walls, possibly as a result of fan/intake coupling.

### 3.2. Parametric study of scarf and contraction ratio at increasing incidence

The results of the initial design space exploration were used to identify restricted ranges for the design variables to be used in the successive investigations at increasing angle of attack. The low degree of correlation of the reported metrics with the lip aspect ratio at both top and bottom sections suggested to avoid a direct specification of this parameter. The following analysis was carried out considering only CR and  $\sigma$  as independent variables.

In generating the intake shapes, a particular attention was devoted to the application of scarf. The DOE analysis highlighted the tendency of decreased performance for larger  $\sigma$  values. In the parametric study, where the lip AR was not explicitly imposed, the throat section displacement as a result of inlet scarfing was set in order to avoid the appearance of overly bent diffuser lines towards the bottom dead centre. This required reducing the throat length  $a$  of Fig. 6(a) as  $\sigma$  increased. The results reported in the following are related to this design groundrule.

The two geometric variables down-selected in the DOE with their corresponding ranges were analysed in a grid-search exploration at the three incidence angles of  $16^\circ$ ,  $24^\circ$ , and  $28^\circ$ . An equispaced grid with 7 values of  $\sigma$  in  $[-3.0, 6.0]$  and 4 values of CR in  $[1.165, 1.27]$  was chosen to sample the design space, giving a total of 28 points. The computed distribution of performance indexes at equalised mass flow are presented in the following. As outlined in Section 2.2, we compared two standard metrics related to the total intake losses (IPR) and the stagnation pressure distortion (DC(60)), with the delta index of Gunn for the stagnation pressure ( $\bar{D}_m(p_0)$ ) and absolute swirl ( $\bar{D}_m(\alpha)$ ).

The parametric plots of Figs. 8(a)-8(c) report the metric distributions as a function of the scarf angle  $\sigma$  for constant CR values. For each angle of attack, the combination giving the optimal value for the different metrics and the influence exerted by the design variables can be identified.

At  $AOA = 16^\circ$ , the effect of the scarf angle on the total pressure is enhanced when the contraction ratio is greater than 1.20. Below this CR, the curves are flat. IPR presents a maximum for  $CR = 1.20$  and  $\sigma = 1.5^\circ$  and reduces for larger contraction ratios. The total pressure distortion metrics highlight an almost monotonic increasing influence of CR and a more complex trend for the scarf angle. DC(60) and  $\bar{D}_m(p_0)$  feature a similar distribution and they both reach a minimum for  $\sigma$  around  $3^\circ$ . When  $\sigma > 3^\circ$  and  $CR > 1.20$ , they rapidly grow

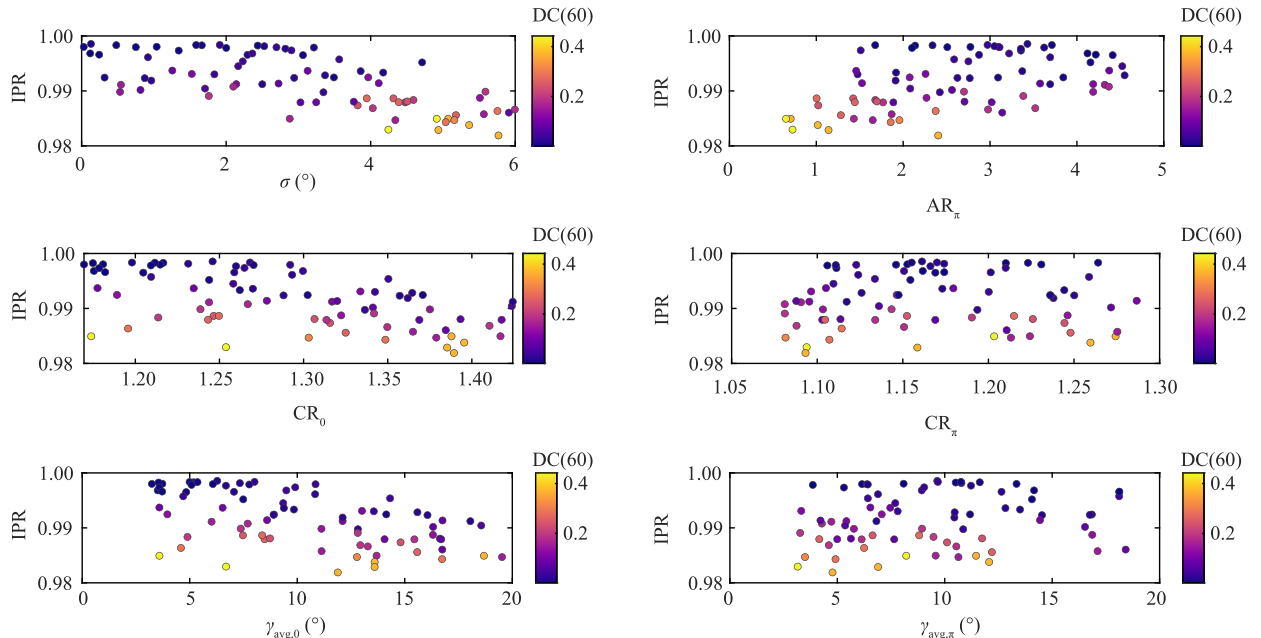
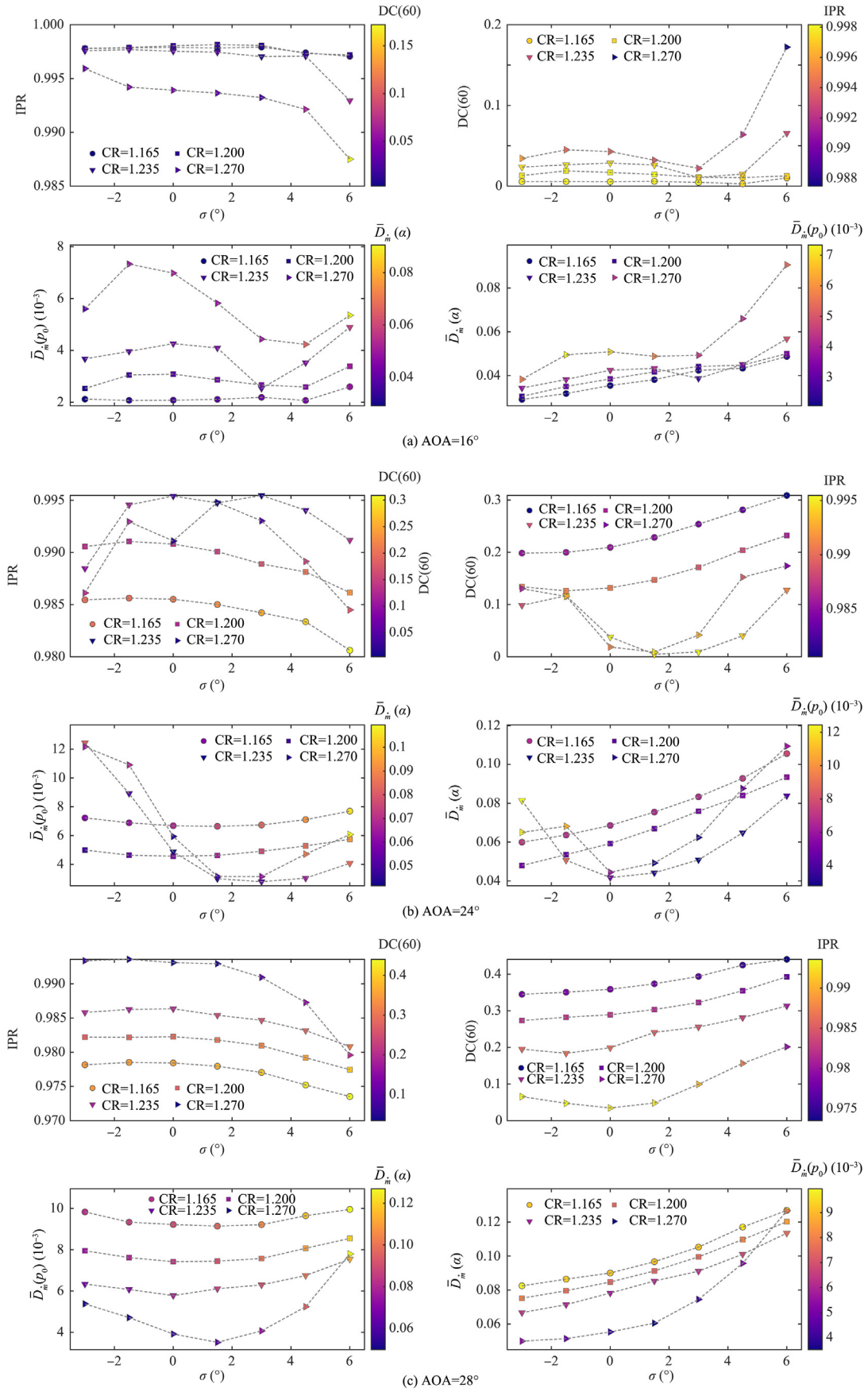


Fig. 7 Distribution of IPR and DC(60) metrics vs geometric parameters in initial design space exploration at  $AOA = 16^\circ$ .



**Fig. 8** Parametric variation of performance metrics at increasing incidence.

as a small separation starts to form. The worst performance is obtained for  $CR = 1.270$ . In this case, an axisymmetric loss occurring in the diffuser for low  $\sigma$  values is detected only by  $\bar{D}_m(p_0)$ , that activates more than DC(60). The absolute swirl index  $\bar{D}_m(x)$  resembles DC(60), but grows almost linearly with the scarf.

At  $AOA = 24^\circ$ , the distributions show an even netter separation according to the contraction ratio and two distinct behaviours are present in Fig. 8(b). When  $CR \leq 1.20$ , the intakes have a separated region on the AIP. The curves are smooth and indicate that reducing the scarf angle up to negative values improves the total pressure profile and decrease the swirl variation from the clean case. When  $CR > 1.20$ , there exist a range of  $\sigma$  giving an attached inlet, approximately in  $[-1.0^\circ, 3.0^\circ]$ , whose precise bounds depend upon  $CR$ . Outside this interval, all metrics quickly deteriorate.

At the highest AOA of  $28^\circ$ , reported in Fig. 8(c), the threshold of separation is  $CR > 1.235$ . Below, all inlet models feature a recirculation region at the AIP and the variation of the metrics resembles that at the previous incidence, with smooth curves gently improving as the contraction ratio grows. The curve corresponding to  $CR = 1.27$  shows a different evolution because the inlets are attached in  $\sigma = [-3.0^\circ, 3.0^\circ]$ . Within this interval, IPR is flat and its maximum occurs at  $\sigma = -2.0^\circ$ . DC(60) instead has a minimum for zero scarf, while  $\bar{D}_m(p_0)$  for  $\sigma = 1.5^\circ$ . Proceeding towards higher scarf angles, the delta descriptors surge as the separation builds up.

The compatibility between the intake and the fan in terms of thrust level was assessed by monitoring the isentropic axial thrust coefficient  $CF_x$  throughout the AOA sweep. Fig. 9 illustrates its dependency on the contraction ratio and the scarf angle. The two-dimensional maps reflect the corresponding IPR distributions. At a given mass flow,  $CF_x$  depends on the stagnation pressure downstream of the rotor, which is given by the losses occurring in the intake duct and the rotor compression. The best geometries in terms of thrust are those providing the fan with the largest total pressure that is increased across the blade row up to meeting the design level. The previous graphics of Figs. 8(a)-8(c) indicate that the minimum distortion tends to occur in a region where IPR is close to maximum. Since IPR was found to correlate well with  $CF_x$ , this suggests that the combination of geometric variables can be chosen to provide a high thrust with low distortion at a given incidence.

### 3.3. Analysis of flow field

The figures previously examined indicated a diverse influence of the independent geometric variables studied on the metrics at different incidence. At  $AOA = 16^\circ$ , the impact of the scarf angle on the total pressure field intensifies when  $CR > 1.20$  and is not monotonic. Its effect on the flow field is depicted in Fig. 10, illustrating the Mach number contours on a vertical plane containing the top and bottom dead centres for three inlets with the same contraction ratio of 1.270 and an increasing scarf angle. For  $\sigma = -1.5^\circ$ , the distribution is smooth and the boundary layer grows in the last part of the diffuser. The stream accelerates in the lower lip past the leading edge and a shock wave forms in the throat plane when  $\sigma = 3.0^\circ$ . More downstream, the flow slightly detaches close to the fan tip, driven by excessive diffusion. However, the redistribution of the

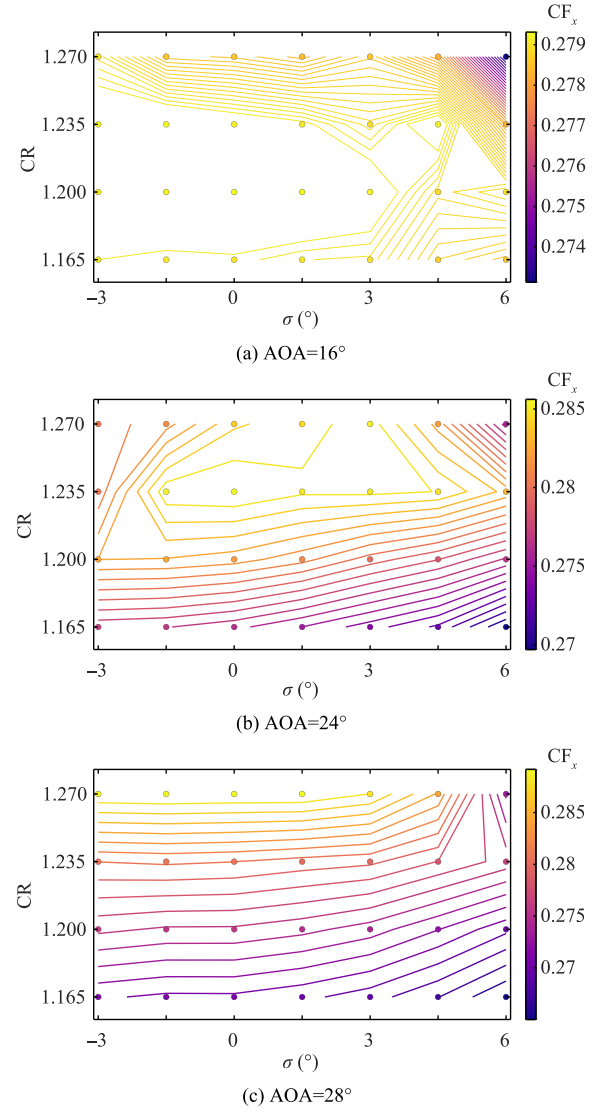


**Fig. 9** Isentropic thrust coefficient vs contraction ratio and scarf at different angles of attack.

inlet area improves the flow on the crown, reducing the throat Mach number and the boundary layer thickness. The average total pressure distortion is therefore reduced. With the largest scarf angle of  $6.0^\circ$ , the shock strength is enhanced and combines with the high diffuser slope to cause a separation bubble, captured by the deteriorated metrics. In the geometries with low contraction ratios, the scarf sensitivity is attenuated because the shock wave appears close to the leading edge and the diffusion-driven separation is dimmed by the fan suction.

In the  $24^\circ$  incidence case, we have highlighted a different behaviour according to the contraction ratio, as values below 1.20 always produced a separated intake. When attached, the scarf angle has a great influence on the metrics. Fig. 11 reports the Mach number distribution for  $CR = 1.235$  at increasing  $\sigma$ . For the negatively scarfed geometry of Fig. 11(a), a recirculation grows in the diffuser duct in the lower lip, triggered by the leading edge shock. When  $\sigma$  is increased to  $1.5^\circ$ , the flow in the bottom section is attached in the throat point and separates

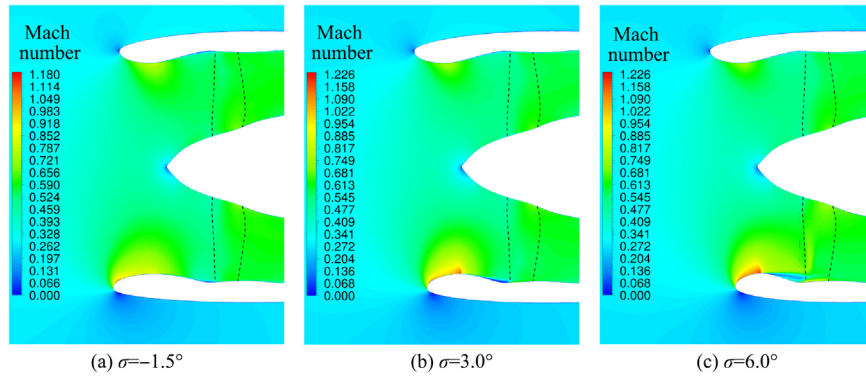


**Fig. 10** Mach number contour at  $\text{AOA} = 16^\circ$  for  $\text{CR} = 1.270$  and increasing scarf angle on a vertical plane cutting the three-dimensional nacelle.

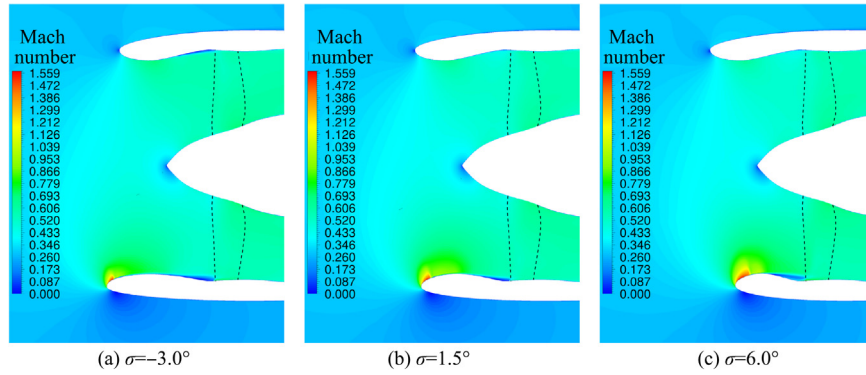


**Fig. 11** Mach number contour at  $\text{AOA} = 24^\circ$  for  $\text{CR} = 1.235$  and increasing scarf angle on a vertical plane cutting the three-dimensional nacelle.

again in the diffuser, but the bubble size is limited by the shorter length and the enhanced fan interaction. However, a further increase of the scarf enlarges the wall angle  $\gamma$  and leads to a detachment that is not removed by the fan. The recirculation when  $\text{CR} < 1.20$  is instead due to the overly thin nose radius that the flow has to circumvent and the appearance of a shock wave very close to the leading edge, inducing a large head separation.

At the largest simulated incidence of  $28^\circ$ , only some intakes with  $\text{CR} = 1.27$  are attached, according to the scarf angle. The surface distribution of isentropic Mach number  $Ma_{\text{iso}}$  and axial skin friction coefficient  $C_{f,x}$  for this  $\text{CR}$  value are illustrated in Fig. 12. The black line represents the throat position. As indicated by the corresponding curve in Fig. 8(c), the metrics present an extremum on the investigated scarf angle interval. In all cases, a shock wave appears in the intake lip around  $\theta = 180^\circ$ , which corresponds to the bottom dead centre. The position and extent of the discontinuity are influenced by the local  $L/D$  ratio determined by the scarf angle. As  $\sigma$  grows towards higher values, the location moves downstream, closer to the throat section. For  $\sigma \geq 1.5^\circ$ , the flow further reaccelerates and a second shock is triggered. The fan interaction can be identified by the increase of  $Ma_{\text{iso}}$  near the fan face around the keel section when the local length is reduced.

The effect of the discontinuity is different, as it can be inferred by the axial skin friction coefficient distribution. At  $\sigma = -3.0^\circ$ , it induces a separation. The flow reattaches before

the throat but is again detached close to the fan face, such that a casing recirculation involving about half of the circumference is present. This can be appreciated in Fig. 13, where the AIP distributions of the difference between the clean ducted case and the high-incidence intake case are shown. The absolute value integral of these quantities gives the delta descriptors. With zero scarf, the post-shock detachment is smaller, but the bubble size at the AIP is approximately of the same size as before, driven by the wall diffusion. The flow for  $\sigma = 1.5^\circ$  is more symmetric. The shock creates a small semicircular separation that reattaches. However, in the diffuser the recirculation expands along the circumference and the AIP bubble enlarges. The greatest scarf angle induces a much larger separation, triggered by a strong shock wave close to the throat and the high  $\gamma$  angle. The flow downstream is highly nonuniform and the AIP bubble is thicker and wider.

The effect of the scarf in terms of flow direction distortion is also represented in the bottom row of Fig. 13. The non-homogeneous distribution derives from the combination of pressure gradient along the vertical direction and rotor mass flux redistribution. Since the fan rotation is counter-clockwise in the figures and opposite to the  $\theta$  direction, a positive absolute swirl angle change  $\Delta\alpha$  corresponds to a counter-swirl, while a negative  $\Delta\alpha$  to a co-swirl. The scarf tends to increase the swirl distortion due to the enhanced flow turning as the  $L/D$  ratio is reduced. The increment is insensitive to the contraction ratio for the separated inlets at higher angles of attack. In fact, far

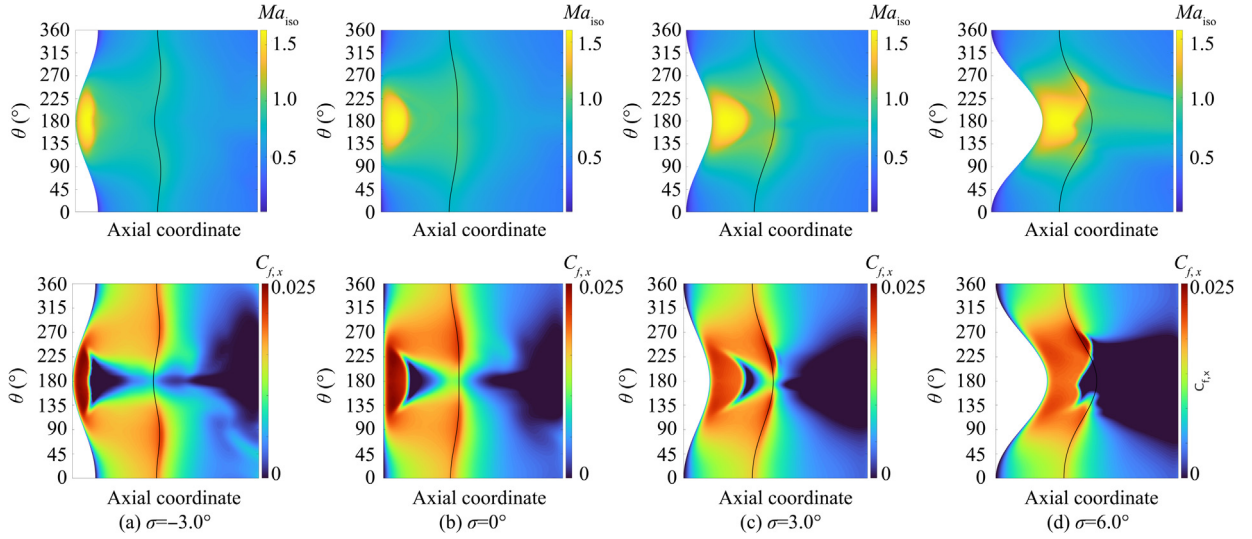


**Fig. 12** Surface distributions for  $CR = 1.27$  and different scarf angles at  $AOA = 28^\circ$ .

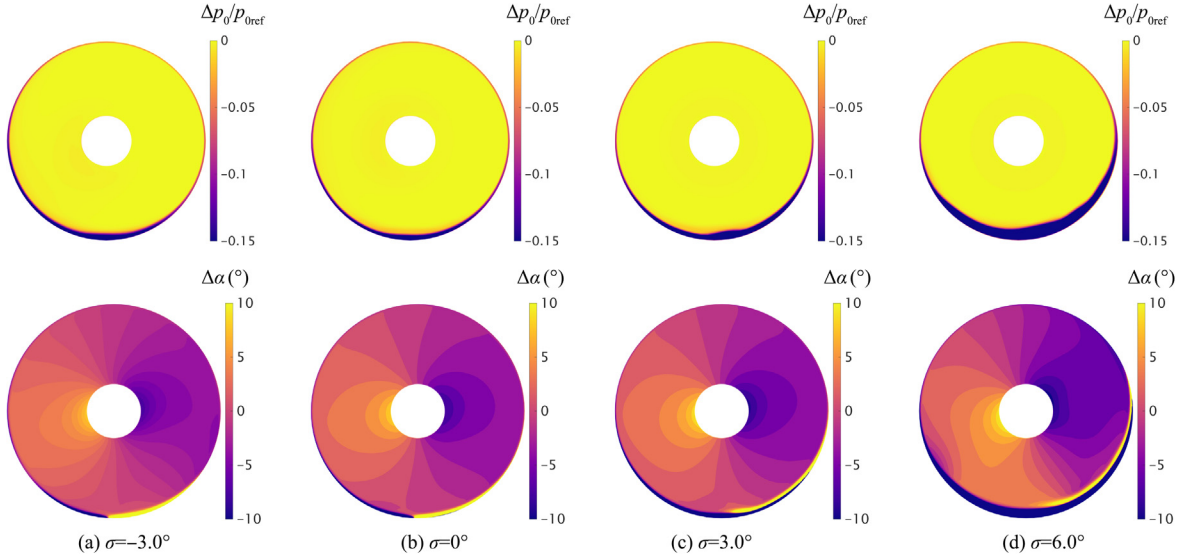


**Fig. 13** AIP flow for  $CR = 1.27$  and different scarf angles at  $AOA = 28^\circ$ .

from the recirculation bubble the swirl distribution is quite similar for all cases and moderately influenced by the free-stream angle of attack. The growth of the separation area and its associated blockage inducing an axial velocity overshoot is progressive and results into a smooth increase of the swirl descriptor. The modified velocity triangle changes the local incidence angle at the blade leading edge. Co-swirl and higher axial velocity decrease the incidence and push the fan towards the choking, whereas counter-swirl and decreased axial velocity drive the fan towards the stall.

#### 3.4. Fan operation under separated intake

The coupled flow analysis allows to consider in addition to the intake metrics also the operation of the fan under the distorted inflow. The most critical case found is  $CR = 1.165$ ,  $\sigma = 6.0^\circ$  at  $AOA = 28^\circ$ , where the inlet distortion is the largest. The corresponding total pressure and axial velocity ( $V_x$ ) distributions pre-

dicted by the body force model upstream and downstream of the fan are shown in Fig. 14. The reference values used for normalisation are the mass-flow averaged quantities obtained in the clean ducted case at the same axial location. The upstream plane is divided in six sectors of equal circumferential amplitude, whose boundaries downstream of the rotor are found by streamline tracking. The inlet separation is centred on Sector 1 and also involves Sectors 6 and 2, with an overall total pressure bubble of  $120^\circ$  near the casing. The orbit plots of total pressure ratio and isentropic efficiency on a per sector basis shown in Fig. 15 against the corrected mass flow  $\dot{m}_c$ , with values normalised by the ducted clean case, help understanding the fan operating condition. Sector 1 has the lowest pressure ratio and mass flow. Its boundary near the tip is smeared due to the negative axial velocity and covers an amplitude close to that of the inlet distortion. In Sector 2, the blades recover the compression up to 70% of the span. In the part of the Sector reaching the casing and circumferentially overlapped with Sector 3, the low axial velocity brings a

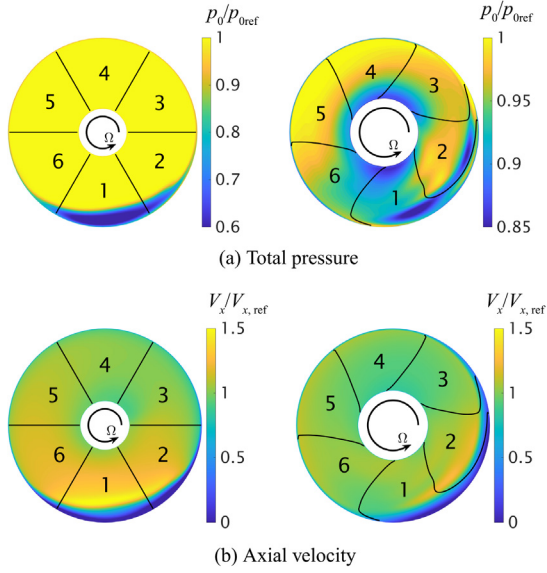


**Fig. 14** Total pressure and axial velocity distribution upstream (left) and downstream (right) of rotor for  $CR = 1.165$  and  $\sigma = 6.0^\circ$  at  $AOA = 28^\circ$ .

large incidence that pushes the blade tips towards the stall. This introduces a high pressure rise and an enlarged loss generation, whose combination leads to the lowest isentropic efficiency value based on the Sector mass flow average, as reported in Fig. 15(b). The low tip velocity remains also in Sector 3, which is affected by the distortion trace mostly close to the shroud. The flow field improves in Sectors 4 and 5, the latter featuring a low circumferential variation with a radial profile closest to the clean case. In both Sectors 5 and 6, the upward flow opposes to the blade rotation to give a counter-swirl. However, the effect on the relative velocity angle is compensated by the average higher axial velocity caused by the bubble blockage, such that the incidence variation is negative and the mass flow increases. The total pressure rise drops approaching the distortion. Overall, the global operating point reported as a black diamond in Fig. 15 shows a compression and efficiency loss of about 4%, relative to the clean ducted case.

### 3.5. Comparison with decoupled approach

All results presented so far were derived considering the coupling between the fan and the intake through the body force method. As explained in the introduction, modelling this

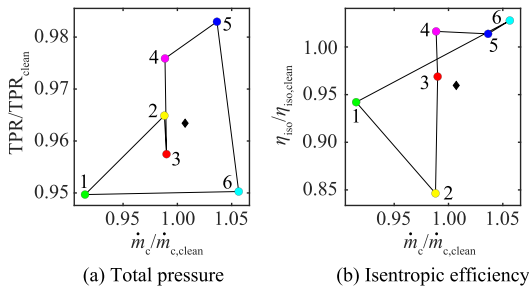


**Fig. 15** Normalised total pressure and isentropic efficiency orbits for  $CR = 1.165$ ,  $\sigma = 6.0^\circ$  at  $AOA = 28^\circ$  (the mass-flow averaged operating point is indicated by the black diamond).

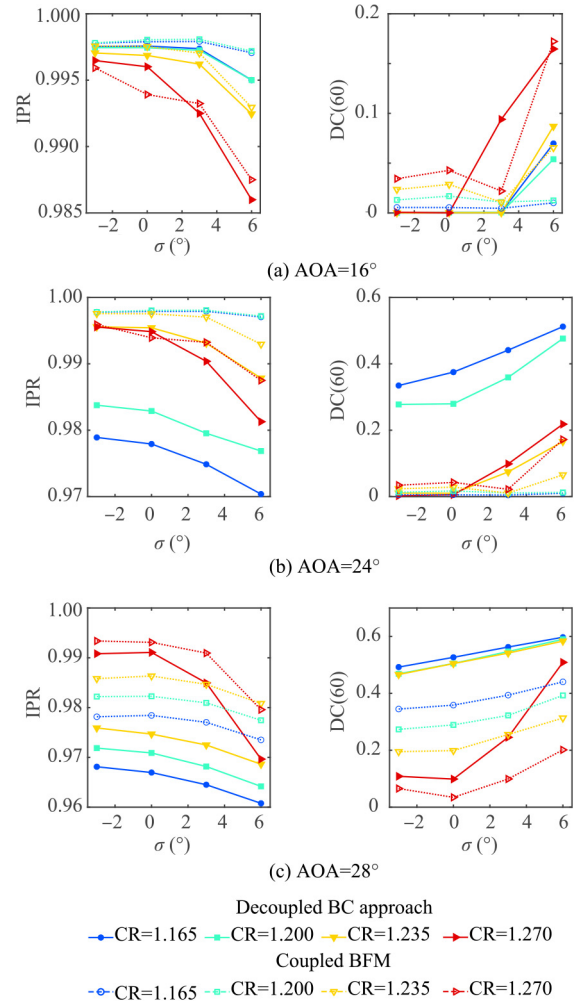


**Fig. 16** Parametric plot of IPR and  $DC(60)$  vs scarf and contraction ratio at increasing incidence (solid lines with full symbols denote the decoupled BC approach, dashed lines with empty symbols the coupled BFM).

interaction has been recognised to be unavoidable to obtain physically sound predictions of the flow field, especially for short intakes. Nonetheless, it is interesting to compare the simulations outcome with and without the BFM in the cases analysed during this study, where different geometries were tested. A subset of the individuals examined in Section 3.2 was therefore computed with the BFM inactive. Since no fan coupling was present and its effect was only prescribed as an outlet mass flow from the nozzle, the approach is denoted as Boundary Conditions (BC). Given the geometric symmetry of the nacelles along a vertical plane, the analyses were run with the BFM mesh halved along this plane.

Fig. 16 reports the variation of IPR and  $DC(60)$  with the scarf angle, parametric with respect to the contraction ratio. Solid lines with full symbols denote the BC results, while dashed lines and empty symbols indicate the BFM results, previously shown in Figs. 8(a)-8(c). Some interesting features can be inferred from the plot. In general, when the inlet is attached, the BFM predicts a higher IPR and  $DC(60)$ . The fan redistributes the flow improving the total pressure losses, but also

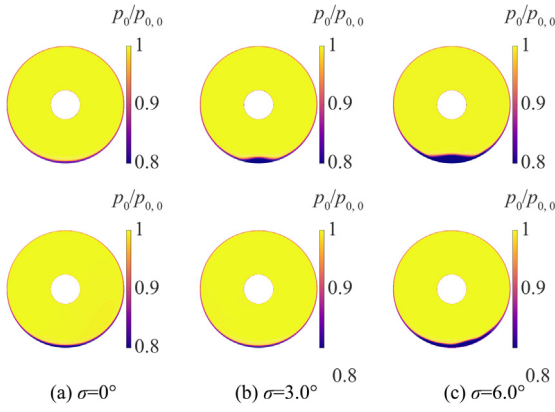


**Fig. 17** Comparison of relative total pressure on AIP at AOA = 24° and CR = 1.235 (top row is BC, bottom row is BFM).

adding more non-uniformity, compared to the BC case. The separation in the coupled operation builds up more smoothly, whereas it is more abrupt when the fan is not modelled. It is in fact known that the rotor exerts a suppression effect delaying the flow detachment, compared to a flow-through nacelle. However, the curves indicate that even at the same incidence, the correspondence between the BC and the BFM depends on the intake design. For instance, at AOA = 16°, Fig. 16(a) shows that the BC predicts the separation in all geometries with  $\sigma > 3^\circ$ , whereas that only occurs for CR > 1.20 in the BFM. Similarly, at AOA = 24° all intakes with CR < 1.23 are stalled with the BC, but for a higher contraction ratio that only happens for  $\sigma > 0^\circ$ . Conversely, the BFM shows separation only at  $\sigma = 6^\circ$ . The points presenting a recirculation with the BFM, instead, are equally separated also with the BC. In these cases, the discrepancy with the BFM metric levels is large (about -0.01 for IPR and +0.3 for DC(60)), but the two sets of curves present similar trends.

Apart from the values of the indicators, the difference between the two approaches can be appreciated by looking at the flow field on the AIP. Fig. 17 compares the total pressure normalised to freestream value at AOA = 24° and CR = 1.235, for three scarf angles. In the BC cases shown in the top row, a small recirculation grows near the bottom dead centre as the scarf is increased. Conversely, in the BFM simula-

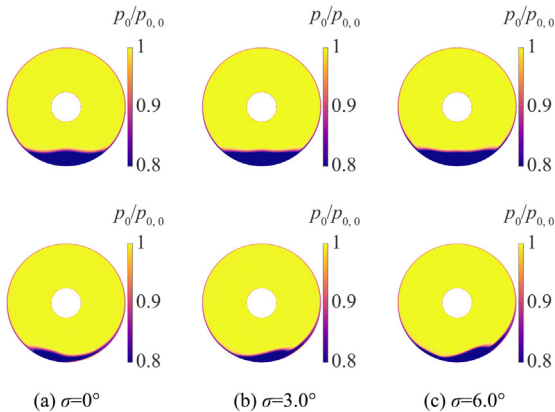


**Fig. 18** Comparison of relative total pressure on AIP at AOA = 28° and CR = 1.235 (top row is BC, bottom row is BFM).

tions of the bottom row the boundary layer first becomes thinner from  $\sigma = 0^\circ$  to  $\sigma = 3.0^\circ$ , and then a smeared separation appears.

The same geometries are fully separated at AOA = 28°. In such cases, the BC always largely overpredicts the extent of the flow recirculation, as highlighted by the large discrepancy of the performance metrics and illustrated in Fig. 18.

#### 4. Conclusions

The parametric intake geometry study highlighted several features of fan/inlet interaction for the nominal  $L/D = 0.35$  case study at increasing incidence angle. The main conclusions regarding the two independent variables examined, the scarf angle and the contraction ratio, can be summarised as:

- (1) The contraction ratio determined the threshold for inlet separation. According to the incidence, increasing values of CR were needed to avoid flow detachment: CR > 1.20 at 24°, and CR > 1.24 at 28°.
- (2) The effect of the scarf angle depended upon the inlet regime: if attached, an optimal region was found from 0° to 3°; with a flow detachment, lowering the scarf up to negative values improved all metrics.

Considering the performance metrics adopted:

- (1) DC(60) has been already recognised not to represent the real distortion level for complex patterns. In many points,  $\bar{D}_m(p_0)$  predicted a more spoiled inflow, for instance when the total pressure deviation extended widely along the circumference.
- (2) The axial swirl distortion measured by  $\bar{D}_m(x)$  was proportional to the scarf angle and in turn to the  $L/D$  ratio on the bottom lip section, confirming that shorter ducts enhanced the potential flow distortion;
- (3) The axial thrust coefficient correlated with IPR and the fan TPR distribution in the simulated cases; therefore, the thrust requirement could be monitored by considering the IPR in the first place.

With regards to the fan modelling in the numerical simulations:

- (1) When included through the BFM, the fan suppressed the separation relative to the decoupled case depending on both the intake design and the incidence angle;
- (2) In case an attached inlet is predicted both with and without the fan model, the total pressure recovery and the DC(60) index were in general higher in the first case;
- (3) For fully separated configurations, the size of the recirculation was much larger in the decoupled simulation; in this condition, the performance metrics exhibited the greatest difference.

The indications coming from this study in terms of suitable geometric variable ranges derive from the operating condition selected, the highlight area and droop angles, and the groundrules used to generate the intake models. The individuals examined can present sub-optimal features, since they were

generated out of a parametric analysis. On the other hand, a coupled three-dimensional optimisation of the inlet surface for each of them is not feasible. Specifying different values along the circumference can also provide a performance improvement and might be part of a successive design refinement. Finally, other operating conditions are likely to prefer different intake geometries. Given the multi-point nature of the problem, for a more complete overview the study can be extended to the examination of additional operating points, like cruise or crosswind, where other lip features are required to achieve an optimal performance.

### Declaration of Competing Interest

The authors declare that they have no known competing financial interests or personal relationships that could have appeared to influence the work reported in this paper.

### References

- Owens R, Hasel K, Mapes D. Ultra high bypass turbofan technologies for the twenty-first century. Reston: AIAA; 1990. Report No.: AIAA-1990-2397.
- Hughes CE. Aircraft engine technology for green aviation to reduce fuel burn. Reston: AIAA; 2011. Report No.: AIAA-2011-3531.
- Graham WR, Hall CA, Vera Morales M. The potential of future aircraft technology for noise and pollutant emissions reduction. *Transp Policy* 2014;**34**:36–51.
- Magrini A, Buosi D, Benini E, et al. Ultra-high bypass nacelle geometry design space exploration. Reston: AIAA; 2021. Report No.: AIAA-2021-0990.
- Peters A, Spakovszky ZS, Lord WK, et al. Ultrashort nacelles for low fan poressure ratio propulsors. *J Turbomach* 2015;**137**(2): 021001.
- Hodder B. An investigation of engine influence on inlet performance (conducted in the Ames 40- by 80-foot wind tunnel). Washington, D.C.: NASA; 1981. Report No.: NASA-CR-166136.
- Larkin MJ, Schweige PS. Ultra high bypass nacelle aerodynamics. Washington, D.C.: NASA; 1992. Report No.: NASA-CR-189149.
- Motycka DL. Reynolds number and fan/inlet coupling effects on subsonic transport inlet distortion. *J Propul Power* 1985;**1**(3):229–34.
- Coschignano A, Babinsky H, Sheaf C, et al. Influence of near-leading edge curvature on the performance of aero-engine intake lips at high-incidence. Reston: AIAA; 2016. Report No.: AIAA-2016-3559.
- Coschignano A, Babinsky H, Sheaf C, et al. Effect of lip shape on shock wave-boundary layer interactions in transonic intakes at incidence. Reston: AIAA; 2019. Report No.: AIAA-2019-1844.
- Kennedy S, Robinson T, Spence S, et al. Computational investigation of inlet distortion at high angles of attack. *J Aircraft* 2014;**51**(2):361–76.
- Cao T, Vadlamani NR, Tucker PG, et al. Fan-Intake interaction under high incidence. *J Eng Gas Turbines Power* 2017;**139**(4):041204.
- Vadlamani NR, Cao T, Watson R, et al. Toward future installations: mutual interactions of short intakes with modern high bypass fans. *J Turbomach* 2019;**141**(8):081013.
- Mohankumar B, Hall CA, Wilson MJ. Fan aerodynamics with a short intake at high angle of attack. *J Turbomach* 2021;**143**(5):051003.
- Gunn E, Brandvik T, Wilson MJ. Fan-intake coupling with conventional and short intakes. New York: ASME; 2021. Report No.: GT 2021–58829.
- Zhang W, Vahdati M. A parametric study of the effects of inlet distortion on fan aerodynamic stability. *J Turbomach* 2019;**141**(1):011011.
- Greitzer EM, Mazzawy RS, Fulkerson DA. Flow field coupling between compression system components in asymmetric flow. *J Eng Gas Turbines Power* 1978;**100**(1):66–72.
- Peters A. Ultra-short nacelles for low fan pressure ratio propulsors [dissertation]. Cambridge: Massachusetts Institute of Technology; 2014.
- Ma Y, Cui J, Vadlamani NR, et al. Effect of fan on inlet distortion: Mixed-fidelity approach. *AIAA J* 2018;**56**(4):2350–60.
- Carnevale M, Wang F, Parry AB, et al. Fan similarity model for the fan-intake interaction problem. *J Eng Gas Turbines Power* 2018;**140**(5):051202.
- Godard B, De Jaeghere E, Ben Nasr N, et al. A review of inlet-fan coupling methodologies. New York: ASME; 2017. Report No.: GT 2017–63577.
- Burlot A, Sartor F, Vergez M, et al. Method comparison for fan performance in short intake nacelle. Reston: AIAA; 2018. Report No.: AIAA-2018-4204.
- Godard B, De Jaeghere E, Ben Nasr N, et al. Methodologies for turbofan inlet aerodynamics prediction. Reston: AIAA; 2017. Report No.: AIAA-2017-3413.
- Benichou E, Dufour G, Bousquet Y, et al. Body force modeling of the aerodynamics of a low-speed fan under distorted inflow. *Int J Turbomachinery, Propulsion Power* 2019;**4**:8–12.
- Magrini A, Benini E, Yao HD, et al. A review of installation effects of ultra-high bypass ratio engines. *Prog Aerosp Sci* 2020;**119**:100680.
- Yeung A, Vadlamani NR, Hynes T, et al. Quasi 3D nacelle design to simulate crosswind flows: Merits and challenges. *Int J Turbomachinery, Propulsion Power* 2019;**4**:25.
- John A, Bower J, Qin N, et al. Using shock control bumps to improve engine intake performance and operability. *Aeronaut J* 2020;**124**:1913–44.
- Wang S, Cao C, Wang C, et al. A nacelle inlet design approach with more three-dimensional geometric consideration. *Aerosp Sci Technol* 2021;**112**:106624.
- Abbott J. Computational study of the aerodynamic performance of subsonic scarf inlets. Reston: AIAA; 2004. Report No.: AIAA-2004-3406.
- Menegozzo L, Benini E. Boundary layer ingestion propulsion: A review on numerical modeling. *J Eng Gas Turbines Power* 2020;**142**(12):120801.
- Hall DK, Lieu M. Propulsor models for computational analysis of aircraft aerodynamic performance with boundary layer ingestion. Reston: AIAA; 2021. Report No.: AIAA-2021-0991.
- Corroyer J, Schnell R. Coupled fan and intake design optimization for installed UHBPR-engines with ultra-short nacelles. *22nd international symposium on air breathing engines*; 2015.
- Magrini A, Buosi D, Benini E. Sensitivity analysis of nacelle intake high-incidence aerodynamics including a body force fan model. Reston: AIAA; 2021. Report No.: AIAA-2021-0606.
- Yildirim A, Gray JS, Mader CA, et al. Coupled aeropropulsive design optimization of a podded electric propulsor. Reston: AIAA; 2021. Report No.: AIAA-2021-3032.
- Spalart P, Allmaras S.A one-equation turbulence model for aerodynamic flows. Reston: AIAA; 1992. Report No.: AIAA-1992-0439.
- Pointwise. *Pointwise user manual*. Forth Worth: Pointwise, Inc.; 2020.
- Re RJ, Abeyounis WK. A wind tunnel investigation of three NACA 1-series inlets at Mach numbers up to 0.92. Washington, D.C.: NASA; 1996. Report No.: NASA-TM-110300.
- Celik IB, Ghia U, Roache PJ, et al. Procedure for estimation and reporting of uncertainty due to discretization in CFD applications. *J Fluids Eng* 2008;**130**(7):0780011.

39. Thollet W. Body force modeling of fan-airframe interactions [dissertation]. Toulouse: Université de Toulouse - ISAE; 2017.
40. Magrini A. Study of body force modelling for coupled fan/airframe simulations [dissertation]. Padova: Università degli Studi di Padova; 2020.
41. Hughes CE. Aerodynamic performance of scale-model turbofan outlet guide vanes designed for low noise. Cleveland: NASA Glenn Research Center; 2001. Report No.: NASA TM-2001-211352.
42. Van Zante DE, Podboy GG, Miller CJ, et al. Testing and performance verification of a high bypass ratio turbofan rotor in an internal flow component test facility. Cleveland: NASA Glenn Research Center; 2009. Report No.: NASA TM-2009-215661.
43. SAE. Inlet total-pressure-distortion considerations for gas-turbine engines. Warrendale: Society of Automotive Engineering; 1994.
44. SAE. Gas turbine engine inlet flow distortion guidelines. Warrendale: Society of Automotive Engineering; 1978.
45. Goldsmith EL, Seddon J. *Practical intake aerodynamic design*. Reston: AIAA; 1993.
46. Magrini A, Buosi D, Benini E. Maximisation of installed net resulting force through multi-level optimisation of an ultra-high bypass ratio engine nacelle. *Aerosp Sci Technol* 2021;**119**:107169.